ACS APPLIED MATERIALS & INTERFACES

Research Article

www.acsami.org

Solvothermal, Chloroalkoxide-based Synthesis of Monoclinic WO_3 Quantum Dots and Gas-Sensing Enhancement by Surface Oxygen Vacancies

Mauro Epifani,*[,†] Elisabetta Comini,[‡] Raül Díaz,[§] Teresa Andreu,[∥] Aziz Genç,[⊥] Jordi Arbiol,[⊥,#] Pietro Siciliano,[†] Guido Faglia,[‡] and Joan R. Morante[∥,⊗]

[†]Istituto per la Microelettronica e i Microsistemi, IMM-CNR, Via Monteroni, 73100 Lecce, Italy

[‡]SENSOR Lab, Department of Information Engineering, Brescia University and CNR-INO, Via Valotti 9, 25133 Brescia, Italy

[§]Electrochemical Processes Unit, IMDEA Energy Institute, Avda. Ramón de la Sagra, 3 28935 Móstoles, Spain

[∥]Catalonia Institute for Energy Research, IREC, c/Jardins de les Dones de Negre 1, 08930 Sant Adria del Besos, Barcelona, Spain

[⊥]Institut de Ciència de Materials de Barcelona, ICMAB-CSIC, Campus de la UAB, 08193 Bellaterra, Spain

[#]Institució Catalana de Recerca i Estudis Avançats, ICREA, Passeig Lluís Companys, 23, 08010 Barcelona, Spain

[⊗]M2E-IN2UB-XaRMAE, Departament d'Electrònica, Universitat de Barcelona, c/Martí i Franquès 1, 08028 Barcelona, Spain

Supporting Information

ABSTRACT: We report for the first time the synthesis of monoclinic WO_3 quantum dots. A solvothermal processing at 250 °C in oleic acid of W chloroalkoxide solutions was employed. It was shown that the bulk monoclinic crystallographic phase is the stable one even for the nanosized regime (mean size 4 nm). The nanocrystals were characterized by X-ray diffraction, High resolution transmission electron microscopy, X-ray photoelectron spectroscopy, UV−vis, Fourier transform infrared and Raman spectroscopy. It was concluded that they were constituted by a core of monoclinic WO_3, surface covered by unstable W(V) species, slowly oxidized upon standing in room conditions. The WO_3 nanocrystals could be easily processed to prepare gas-sensing devices, without any phase transition up to at least 500 °C. The devices displayed remarkable response to both oxidizing (nitrogen dioxide) and reducing (ethanol) gases in concentrations ranging from 1 to 5 ppm and from 100 to 500 ppm, at low operating temperatures of 100 and 200 °C, respectively. The analysis of the electrical data showed that the nanocrystals were characterized by reduced surfaces, which enhanced both nitrogen dioxide adsorption and oxygen ionosorption, the latter resulting in enhanced ethanol decomposition kinetics.

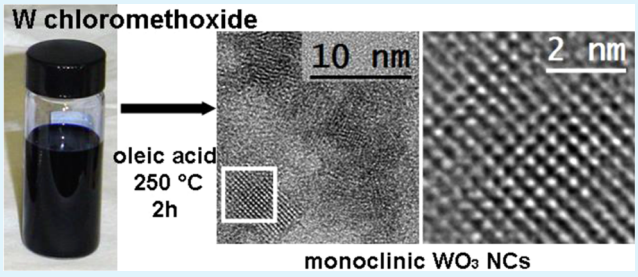

KEYWORDS: *tungsten trioxide, gas-sensing, solvothermal synthesis*

INTRODUCTION

Tungsten trioxide (WO_3) attracts continuously renovated attention, due to its intricate structural properties and, above all, the broad range of applications disclosed by its properties: electrochromic devices,[1−4] gas sensors,[5−14] photoelectrochemical systems,[15−19] supercapacitors,[20−22] batteries,[23−25] pH sensors,[26] just to mention some examples. Further interest has been raised by the possibility of growing an enormous range of WO_3 nanostructures[27] by several synthetic approaches. In wet chemical syntheses, the typical precursors are tungstates[28−30] or WCl_6,[31−36] which are processed in hydrolytic or even water-free[33,34] conditions. The formation of W oxide nanostructures most probably takes place by progressive polymerization of the polyions present in solution. The synthesis products are, very commonly, substoichiometric (like $W_{18}O_{49}$)[37−41] or metastable phases,[42] and the final WO_3 phase can be obtained upon heat treatment.[35,42,43] Only in a few cases the WO_3 phase is directly obtained from the solution synthesis,[37] but only 2D nanostructures have been reported. Surprisingly, there are no reports concerning the direct synthesis of monoclinic WO_3 quantum dots (0D structures). This topic is of remarkable interest: (i) from a fundamental point of view, for investigating the size effect on the properties of WO_3: in particular, for probing the phase stability of WO_3 in the small size regime; (ii) from a synthetic perspective, for understanding whether the chemical properties of the W ions intrinsically exclude the formation of quantum dots. In this paper we show that it is possible to synthesize WO_3 quantum dots by wet chemical approach at low temperature, which allowed the preparation of 4 nm sized nanocrystals. We show

Received: June 26, 2014
Accepted: September 11, 2014
Published: September 11, 2014

that the typical monoclinic crystallographic phase, which is the most stable for bulk WO_3 in ordinary conditions, is kept even for such small size regime. The heat-treated materials were characterized by enhanced surface oxygen vacancy concentration, as evidenced by basic electrical measurements. This property suggested the exploitation of the materials for the preparation of sensing devices, where it is essential to tune the surface chemistry by highly reactive sites like oxygen vacancies. In fact, the sensing properties of the nanocrystals were surprisingly remarkable for both reducing (ethanol) and oxidizing (nitrogen dioxide) gases, with responses ranging over 2−3 orders of magnitude.

EXPERIMENTAL SECTION

Tungsten chloroalkoxide solutions were synthesized from WCl_6 as reported in detail in previous work.[44] For the solvothermal step, 2 mL of the solution was mixed with 10 mL of oleic acid (technical grade), and poured into a 45 mL Parr autoclave. The autoclave was heated for various times ranging from 1 to 4 h at 250 °C into a furnace. Alternative syntheses were carried out by using oleylamine or *n*-dodecanol instead of oleic acid. After the solution was cooled, a blue precipitate was collected by methanol addition and centrifugation, and dried in air at 90 °C.

X-ray diffraction (XRD) measurements were performed on a Panalytical diffractometer working with the Cu Kα radiation (λ = 1.5406 Å) using a Bragg−Brentano geometry.

Fourier Transform Infrared (FTIR) measurements were carried out with a Nicolet 6700 spectrometer in diffuse reflectance setup, after dispersing the sample powders in KBr.

UV−visible (UV−vis) optical absorption spectra on the solutions were measured with a Thermo Fisher Evolution 300 spectrophotometer. Samples were further diluted in methanol. Diffuse reflection (DR) spectra on the powders were measured by using a DRA-EV-300 integrating sphere.

Raman spectroscopy was performed by means of a Jasco NRS-5100 spectrometer with a green laser in a micro-Raman configuration with 100× objective and with a laser power of 10 mW.

X-ray photoelectron spectroscopy (XPS) was performed using a PHI ESCA-5500 instrument working with the Al Kα radiation (1486.6 eV). The powders were fixed on the sample holder with a biadhesive film, giving them a certain amount of surface charging on all of the peak positions of the main narrow scan spectra acquired. They were all properly corrected with respect to the adventitious C 1s present on the surface with respect to the tabulated and literature value of 284.6 eV.

High resolution transmission electron microscopy (HRTEM) analyses of the powders were carried out with a field emission gun microscope (FEI Tecnai F20), working at 200 kV.

The gas-sensing tests were carried out using a standard configuration for resistive sensor measurement, with 300 nm thick Pt-interdigitated (ID) electrodes and a Pt-resistive-type heater printed onto an alumina substrate (size: 2 × 2 mm). The ID electrodes were deposited by UV lithography step. The active ID contact area was 1400 × 1400 μm with the individual ID contact fingers 50 μm wide and separated by 50 μm gaps. Finally, Pt heaters were realized on the backside of the sensor wafers by sputtering a 500 nm Pt layer that was subsequently patterned via lift-off. The deposited heaters had a meander-shaped geometry. For adhesion improvement, a 50 nm Ti layer was predeposited onto the alumina substrate before the Pt deposition. Sensors were fabricated by depositing a paste made by mixing the as-prepared WO_3 nanocrystals with 1,2-propanediol onto the just described substrates. Before measurements, the sensors were kept at a temperature of 400 °C, provided by the sensor heaters, in order to decompose the organic residuals and stabilize the electrical signal. For this aim, and for sensing tests, the sensor devices were placed in a sealed chamber with a constant flux of 0.3 L/min of humid synthetic air (40% RH at 20 °C) into which the desired amount of test gases was mixed. The sensor response was defined as $|G_{gas} - G_0|/G_0$, where G_0 was the sensor baseline electrical conductance in synthetic air and G_{gas} indicated the sensor electrical conductance after exposure to the target gas. The gases tested in the present work were nitrogen dioxide and ethanol, in concentrations ranging from 1 to 5 ppm and from 50 to 500 ppm, respectively. The same devices were used for carrying out conductance measurements in the presence of different oxygen concentrations. For these last measurements, after equilibrating the sensors at a given oxygen concentration, nitrogen was again introduced in the cell in order to recover the pristine conductance value, then the following oxygen injection in the cell was carried out. The sensing devices selected for the gas tests had base conductance values dispersed within 10% of the results showed in the manuscript. In this case, the measured responses were also comprised in such range. Error bars were hence not included in the plots for clarity sake. Repeated experiments under the same operational conditions yielded stable and reproducible sensor responses for several months (estimated uncertainty = ± 10%).

RESULTS AND DISCUSSION

Upon a prolonged stay at room temperature, the chloroalkoxide solutions precipitated a yellow product. It was not further analyzed, but indicated the concrete possibility of producing polymerized W(VI) species from the solution.

Solvothermal conditions were used to force the transformation of the initial solution species to WO_3, and to provide a coordinating environment for controlling the size growth. Nevertheless, finding the proper synthesis conditions required extensive investigation. Figure 1A shows the XRD patterns of

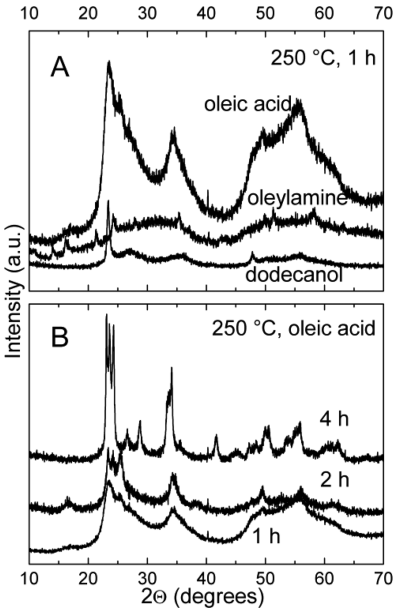

Figure 1. XRD patterns of the samples prepared by heating for 1 h at 250 °C in different solvents (A) and at 250 °C in oleic acid with different heating times (B).

the as-dried samples prepared with various solvents at 250 °C with a fixed heating time of 1 h. The patterns of the samples prepared with oleylamine and dodecanol did not belong to the required WO_3 phase. In particular, the pattern of the sample prepared with dodecanol was typical of $W_{18}O_{49}$ nanorods.[37−41] More interesting was the pattern of the sample prepared with oleic acid after heating for 1 h, which resembled more closely the structure of pure WO_3, in this case recalling the pattern of small tetragonal nanocrystals, as reported recently, but with large differences at high angles.[20] Hence, longer processing

times were attempted for preparing fully crystallized product, and the results are shown in Figure 1B.

After 2 h, the pattern features were resolved, with the most intense peaks slightly shifted to higher angles with respect to the sample heated for 4 h, for which the complete pattern of WO_3 was obtained (JCPDS card 00-043-1035). Moreover, after heating for 2 h, the less intense reflections were not observed, which can be attributed to the small size of the nanocrystals, about 4 nm (see TEM below). As usual, the XRD patterns did not allow distinction between the monoclinic (γ) and triclinic (δ) crystallographic phases of WO_3. TEM results (see below) revealed the presence of the γ phase. In the rest of the work, we will refer to the samples obtained after heating for 2 h. In fact, the Raman data in Figure 2 show that even after heating for 2 h,

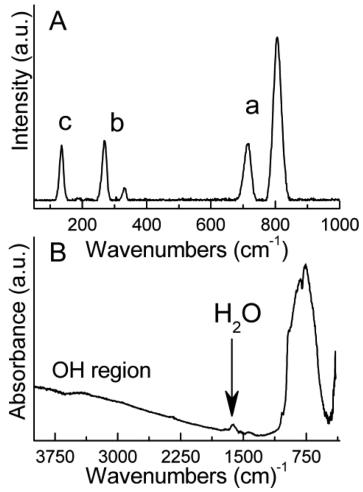

Figure 2. Raman (A) and IR (B) spectra measured on WO_3 sample prepared by heating for 2 h at 250 °C in oleic acid. The Raman regions marked in the figure are described in the text.

the observed bands are in complete agreement with the known modes of WO_3,[45,46] without any obvious difference. The regions indicated in the figure correspond to the usually modes in crystalline WO_3: (a) stretching (ν O−W−O) between 900 and 600, (b) deformation (δ O−W−O) between 400 and 200 and (c) lattice modes of WO_3 below 200 cm^{-1}. This result confirms the interpretation of the XRD data, in particular as concerns the absence of complex tungstate species. Even the IR curve displayed the typical WO_3 bands in the low energy region. More interesting were, aside the water band at 1620 cm^{-1}, the extremely weak features at 1420 and 1530 cm^{-1}, which are due to the formation of oleate complexes.[47−49]

The absence of methyl/methylene bands around 3000 cm^{-1} also helped us to conclude that oleic acid was loosely bonded to the nanocrystal surface and was removed after the purification steps. In the high energy region, OH bands were practically absent, hence solvothermal conditions favored extensive inorganic condensation between the W-containing species. Cheon and co-workers[50] used WCl_4 derived solution to prepare $W_{18}O_{49}$ nanorods by processing in oleylamine and oleic acid solutions. Park and co-workers[51] prepared the same phase starting from $W(CO)_6$ processing in oleylamine. It seems that the presence of oleylamine favors substoichiometric products and/or metastable phases, in agreement with recent work.[20] Even in the present work, the final product (Figure 1) in the presence of oleylamine did not resemble the desired WO_3 phase. Instead, pure oleic acid favored the formation of monoclinic WO_3. Moreover, the just quoted references reported the preparation of colloidal nanostructures, indicating surface capping by oleylamine. The IR spectrum in Figure 2 shows weak binding of oleic acid to the WO_3 nanocrystals, as discussed above. Hence, oleic acid alone acted as a weak size-limiting environment.

This weak capping tendency resulted in the isotropic growth, thus avoiding the formation of nanorods, and, above all, probably allowed more extensive structural reorganization of the nanocrystals into WO_3 structures, with W species achieving the proper final coordination by oxygen ions. This would also explain that, after 4 h at 250 °C, much larger WO_3 nanocrystals were obtained (about 15 nm, as estimated by Scherrer equation). The color of all the as-dried samples was blue, which indicated the formation of reduced tungstates. On the other hand, we have just seen that XRD and other techniques clearly showed the presence of only WO_3. For investigating this puzzling finding, first the color was characterized by optical techniques. The DR UV−vis spectra were compared with that of the yellow WO_3 sample obtained after heating 400 °C. The results are shown in Figure 3. The 400 °C sample displayed an

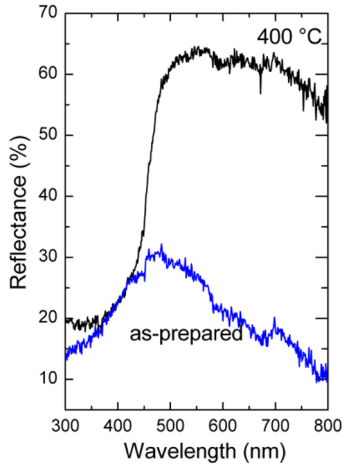

Figure 3. DR UV−vis spectra measured on the indicated samples.

abrupt increase of reflectance above about 400 nm, in agreement with the typical bandgap values for WO_3.[52,53] On the contrary, the reflectance of the as-prepared sample showed a broad maximum centered at about 500 nm, then it rapidly decreased. This result was interpreted by comparing it with the UV−vis spectrum of the starting solution, shown in Figure 4. A

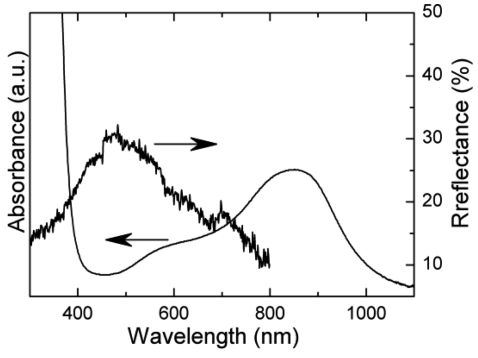

Figure 4. UV−vis absorption and DR spectra measured on the starting solution and the as-prepared sample, respectively.

broad band at about 830 nm, typical of W(V) (d^1 configuration) ions absorption structure,[54−56] confirmed their presence in the solution, resulting from partial reduction of W(VI) by alcohol molecules.[57,58]

Another weaker band at shorter wavelengths indicated the presence of other species, probably with different coordination. The DR spectrum of the as-dried sample had a complementary structure with respect to the solution absorption, which clearly confirmed the relationship between the ions in solution and the surface structure of the WO_3 nanocrystals. Hence, we concluded that the structure of the as-dried materials was constituted by a crystalline WO_3 core covered by W(V) species, which solved the above-described discrepancy. The fact that the blue color became fainted after a few days of standing at room temperature suggested that the W(V) species made a very thin layer around the WO_3 nanostructures. The XPS data also corroborate such a view. The decolored sample (after standing at room temperature for 2 weeks) signal could be fitted with only W(VI) components, as shown in Figure 5. The W $4f_{7/2}$ and W $4f_{5/2}$ peaks were found at 36.0 and 38.1 eV, respectively, which agree with the range of values reported for WO_3.[59−61] The XPS data for the Cl 2p region (Supporting Information) showed complete absence of Cl. Hence, the solution processing resulted in complete solvolysis of the starting W−Cl bonds, improving the material purity. This result is in agreement with the low stability of the W chloroalkoxide solution, due to enhanced hydrolysis of the W precursor.

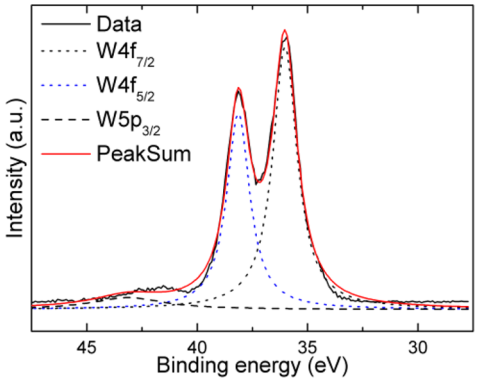

Figure 5. W 4f and W 5p regions of the XPS spectra measured on the sample heated in oleic acid for 2 h at 250 °C.

Figure 6 reports representative HRTEM micrographs on the sample heated in oleic acid for 2 h at 250 °C. In agreement with the FTIR results, showing absence of oleic acid in the sample, the nanocrystals tend to aggregate in ensembles. The nanocrystals had sizes less than 5 nm (about 4 nm in general). Figure 6 also shows a detail of a nanocrystal (white square) and its corresponding power spectrum, which reveals that it is compatible with the monoclinic WO_3 phase (space group = $P2_1/c$) with lattice parameters of a = 0.7301 nm, b = 0.7539 nm and c = 0.7689 nm, and $\alpha = \beta = 90°$ and $\gamma = 90.89°$. It is visualized along the [001] axis. We have found the same WO_3 phase for every nanocrystal we checked. TEM analysis ultimately confirmed the successful preparation of monoclinic WO_3 quantum dots. The processing of sensing devices required thermal stabilization before operating the gas tests. Hence, the thermal behavior of the nanocrystals was investigated after high temperature treatment.

In Figure 7, the XRD patterns of the samples heat-treated at 400 and 500 °C are shown, compared with that of the as-prepared sample. We remind once again that by "as-prepared" we mean the sample prepared by heating at 250 °C in oleic acid for 2 h. It can be seen that only the peak width and intensity were affected, due to the grain growth induced by heat treatments (grain size was about 35 nm mean after heating at 400 °C, as calculated by the Scherrer equation). No obvious changes of the crystallographic phase could be observed. The 400 °C sample was then chosen for the sensing devices

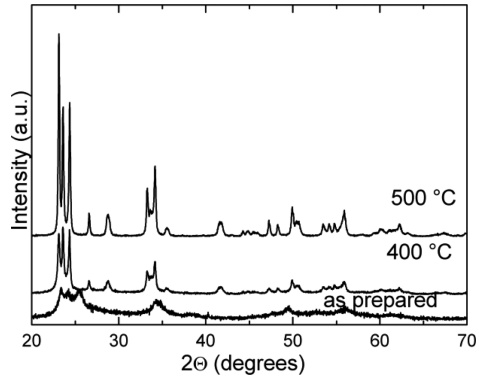

Figure 7. XRD patterns of the WO_3 samples heat-treated at the indicated temperatures.

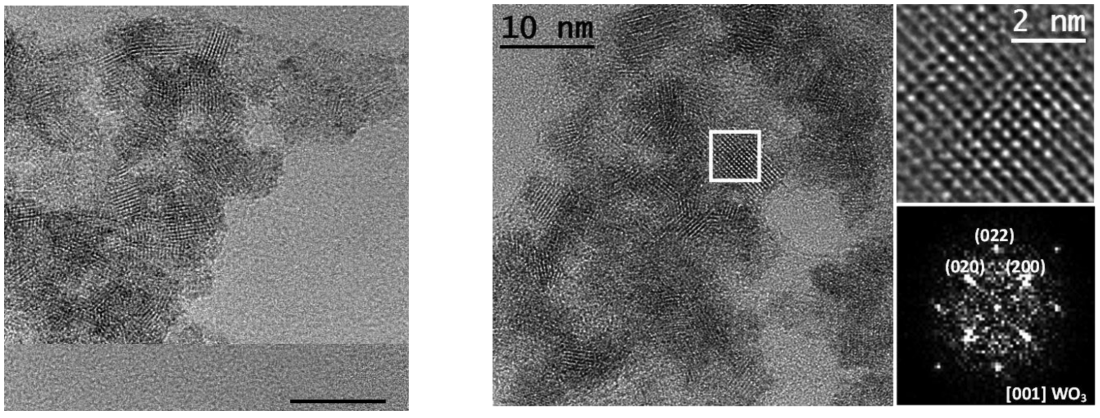

Figure 6. General HRTEM micrographs showing ensembles of about 4 nm spheroidal nanoparticles. Magnified image of a single crystalline nanoparticle and its corresponding power spectrum. The sample was obtained by heating in oleic acid for 2 h at 250 °C.

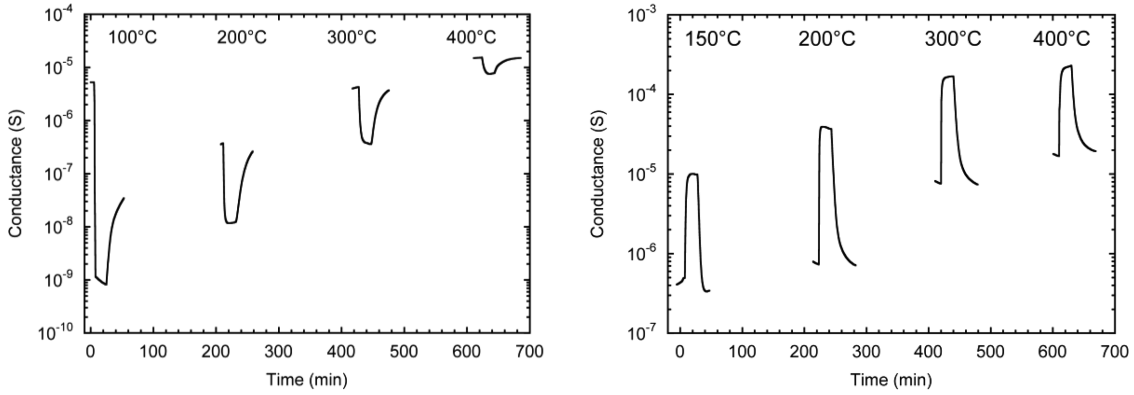

Figure 8. Dynamic response curves of WO_3 sensors to 5 ppm nitrogen dioxide (left) and 500 ppm ethanol (right).

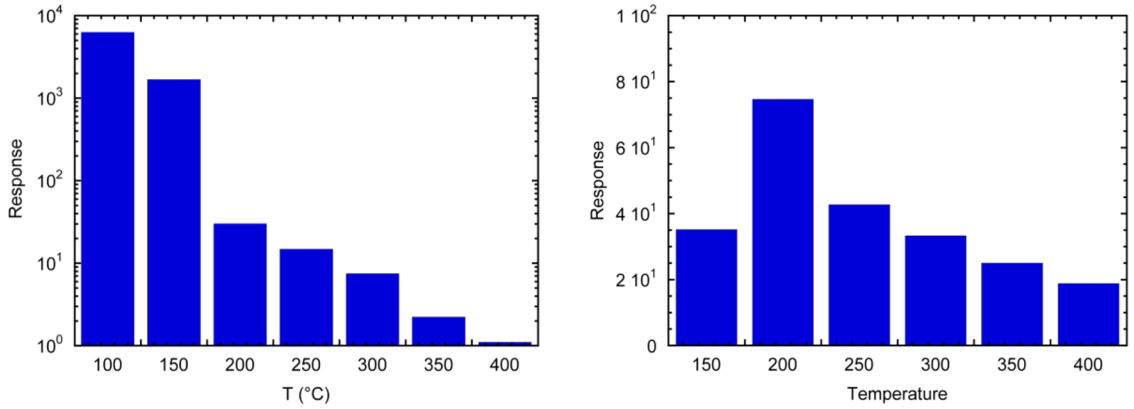

Figure 9. Response vs temperature plots for 5 ppm nitrogen dioxide (left) and 500 ppm ethanol (right).

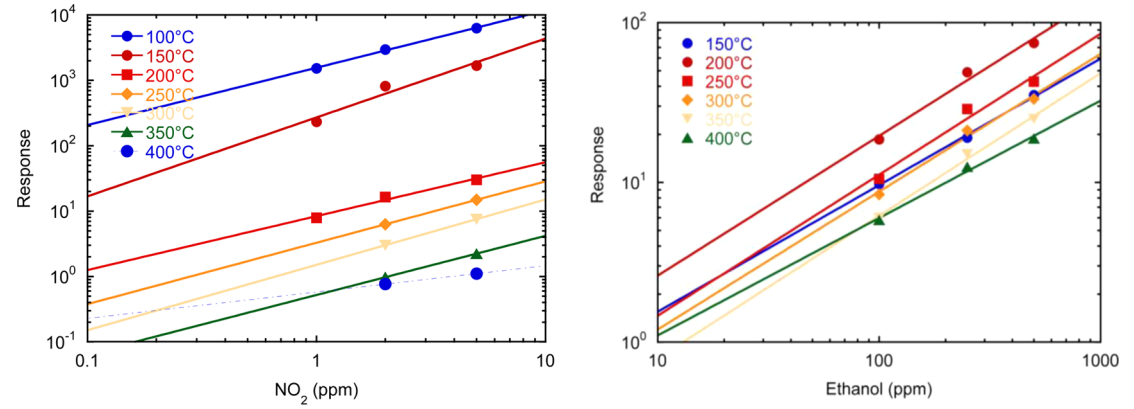

Figure 10. Calibration curves for nitrogen dioxide and ethanol sensing.

processing, because the grain growth was less enhanced than at 500 °C.

Figure 8 shows the dynamic response curves to 5 ppm nitrogen dioxide and 500 ppm ethanol, chosen as oxidizing and reducing gases examples, respectively. The sensors exhibited remarkable conductance variations to both kinds of gases. The sensors showed fast response and recovery, with response and recovery times in the range of 2−5 min and 4−10 min, and 1−2 min and 5−10 min for nitrogen dioxide and ethanol, respectively. The recovery time after testing nitrogen dioxide at 100 °C was much longer, due to the commonly observed persistent adsorption of this gas in such conditions. As expected from the interaction with n-type semiconductor like WO_3, nitrogen dioxide sensing resulted in conductance decrease, contrarily to ethanol. The largest conductance variations for nitrogen dioxide were observed at low operating temperatures, due to the adsorption based sensing mechanism. For ethanol, surprisingly the maximum response occurred at remarkably low operating temperatures: it can be seen in Figure 8 that already at 300 °C the conductance change was less remarked with respect to 200 °C. These qualitative observations were translated into response data, reported in Figure 9 for 5 ppm nitrogen dioxide and 500 ppm ethanol. The response for nitrogen dioxide at 100 °C ranges over almost 4 orders of magnitude of conductance variation, which is an outstanding value for WO_3 sensors. The data for ethanol confirmed that the best performance was obtained at 200 °C, with almost 2 orders of magnitude of conductance increase.

This trend was confirmed by the calibration curves, shown in Figure 10. For each nitrogen dioxide concentration, the response steadily decreased from 100 °C to higher operating temperatures. The extrapolation of the calibration curves showed that the material would even allow detection of subppm concentrations. From the response trend the nitrogen dioxide sensing mechanism can easily be attributed to gas adsorption onto the sensor surface: the slope of the calibration lines ranged around 1, as expected from adsorption based sensing mechanism.[62]

Only for 150 °C, where overlapping NO_2 adsorption and oxygen dissociation mechanisms may be present, the slope rose to 1.2. For ethanol, the highest response was always obtained at a temperature of 200 °C, and the curve extrapolation still shows an appreciable response to 10 ppm of ethanol. The response trends for all concentrations were in agreement with those of Figure 9.

WO_3 is a widespread sensing material, and it has been tested against a broad variety of gases, also including nitrogen dioxide and ethanol. With respect to the best results reported in the literature for nitrogen dioxide,[63−67] the responses that we have measured in the present work are comparable or even larger, despite the heat treatment at 400 °C resulted in grain growth. This was a stimulus to deepen the understanding of the sensing phenomena. Although this task can be extremely complex and needful of a multitechnique approach, it is still possible to draw important indications from the basic electrical properties of the sensing devices. For this reason, simple conductance measurements were carried out at different oxygen concentrations, and the results are shown in Figure 11, replotted in Figure 12 as a

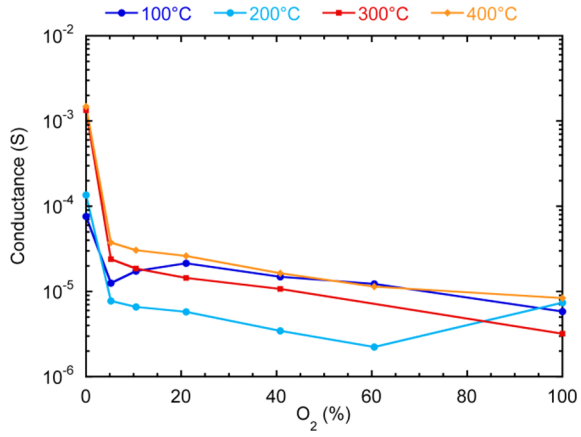

Figure 11. Electrical conductance data of WO_3 nanocrystals heat-treated at 400 °C in the presence of increasing oxygen concentrations.

function of the temperature. The same devices used in the sensing tests were employed for these measurements, hence the nanocrystals were those heat-treated at 400 °C. In Figure 11, it is seen that in pure nitrogen the conductance values increase with increasing the temperature, as expected from *n*-type WO_3.

As soon as oxygen was introduced, the conductance showed a remarkable drop, more and more enhanced with increasing the temperature. This was due to more favored oxygen ionosorption as the temperature was increased.[68] For high oxygen concentrations, the 100 °C measurements were less affected by oxygen adsorption, which takes place at 150−200 °C. For all the operating temperatures, increasing the oxygen concentration resulted in slowly decreasing conductance. If we observe the same data replotted in Figure 12, it is clear that a

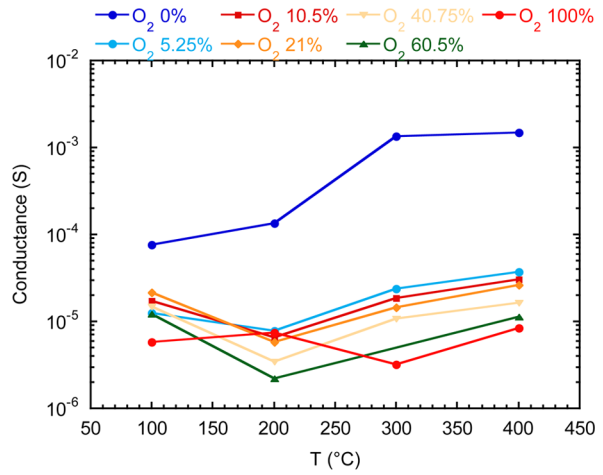

Figure 12. Electrical conductance data of WO_3 nanocrystals heat-treated at 400 °C as a function of the operating temperature.

conductance minimum occurred at about 200 °C. This is a typical effect for many semiconductors and, as explained above, it is easily interpreted as due to the formation of adsorbed O^-.[68] What is important is that, with respect to the curve in pure nitrogen, a huge conductance drop occurred. Oison et al.[69] investigated the interaction between O_3 and WO_3 surface by ab initio methods, concluding that the presence of surface oxygen vacancies is essential for O_3 adsorption and reduction. In their work, the reduction outcome was O adsorption onto WO_3. We can fit their simulation scenario to our case because even for NO_2, adsorption phenomena are at the base of the sensing mechanisms. Hence, we conclude that the electrical data of Figures 11 and 12 indicate the presence of oxygen vacancies, favoring the oxygen ionoadsorption from the surrounding atmosphere and largely influencing the conductance. In particular, the large conductance drop even after introduction of the smallest oxygen concentration allowed supposing the presence of extensively reduced surfaces in our samples. In further studies by Oison et al.,[70] a large concentration of oxygen vacancies resulted in efficient nitrogen dioxide adsorption and, hence, enhanced detection. These consideration helped explaining the huge NO_2 response values obtained in our work, despite the relatively large grain size resulting from the heat treatment at 400 °C. The situation becomes more complex for the ethanol sensing mechanism because it is not straightforward and investigated as deeply as for nitrogen dioxide. It was proposed[71] that ethanol adsorption occurs as ethoxy species, followed by subsequent hydrogen and acetaldehyde desorption. On a stoichiometric surface, adsorption toward surface lattice oxygen cations was proposed. In our case, as seen above, the conductance drop upon injection of small oxygen concentrations revealed that the surface is rich of adsorbed oxygen species. Large conductance variation with respect to pure nitrogen was observed when O concentration of 21% was used (see Figure 12), which was the value in the synthetic air used for gas-sensing tests. We could conclude that the reduced WO_3 surfaces were easily enriched, in the operating conditions, with adsorbed O^- species that favor ethanol adsorption. This is the first rate limiting step in ethanol sensing mechanisms, hence the reduced surface accelerate the ethanol decomposition kinetics just in the temperature range where surface enrichment by adsorbed oxygen is more efficient. Even for ethanol, the need for further understanding the sensing

behavior was stimulated by the remarkable performances, when comparing our results with literature data.[9,11,72−82] The comparison was facilitated by the common use of 100 ppm of ethanol in the sensing tests. First of all, we found that the best operating temperature used in the present work (200 °C) was much lower than the usual values, ranging about 300 °C. Moreover, for such operating temperature, the response values reported in Figure 10 outperform the reported values for many different morphologies and structures (nanoplatelets, nanosheets, nanocubes, etc.). Far from establishing a sterile race for the best performances, this comparison should be stimulating to continuously remind the importance of the surface chemistry in gas sensors. Even after grain growth due to the heat treatment, the sensing performances remain remarkable, and we have established the presence of surface oxygen vacancies as a working hypothesis for detailed mechanism understanding.

CONCLUSIONS

The proper combination of oleic acid and synthesis times can force the W chloroalkoxide precursor species to form cross-linked tungsten oxide products, in the shape of quantum dots and with a crystallographic phase fully ascribable to the bulk monoclinic counterparts. Detailed characterization of the materials showed that the nanocrystal formation most probably occurred by condensation of the precursor species controlled by weak steric hindrance by oleic acid, which mainly modulated the mass transport to the growing species. The prediction about the influence of the surface chemistry of the materials on the remarkable sensing performances was confirmed by the analysis of the conductance data in various oxygen atmospheres. The main feature of the materials was the sensing enhancement attributed to surface oxygen vacancies.

ASSOCIATED CONTENT

Supporting Information

XPS data of the Cl 2p region of the as-prepared sample by heating for 2 h in oleic acid at 250 °C. This material is available free of charge via the Internet at http://pubs.acs.org.

AUTHOR INFORMATION

Corresponding Author

*M. Epifani. E-mail: mauro.epifani@le.imm.cnr.it.

Notes

The authors declare no competing financial interest.

ACKNOWLEDGMENTS

Authors acknowledge CSIC/CNR project 2010IT0001 (SYNCAMON) and the SOLAR project DM19447. We thank Giovanni Battista Pace for the help with the sample preparation, and Nicola Poli for the help with the sensing measurements.

REFERENCES

(1) Deb, S. K. Opportunities and Challenges in Science and Technology of WO_3 for Electrochromic and Related Applications. *Sol. Energy Mater. Sol. Cells* **2008**, *92*, 245−258.

(2) Granqvist, C. G. Electrochromic Tungsten Oxide Films: Review of Progress 1993−1998. *Sol. Energy Mater. Sol. Cells* **2000**, *60*, 201−262.

(3) He, T.; Yao, J. N. Photochromic Materials Based on Tungsten Oxide. *J. Mater. Chem.* **2007**, *17*, 4547−4557.

(4) Wojcik, P. J.; Cruz, A. S.; Santos, L.; Pereira, L.; Martins, R.; Fortunato, E. Microstructure Control of Dual-Phase Inkjet-Printed *a*-WO_3/TiO_2/WO_x Films for High-Performance Electrochromic Applications. *J. Mater. Chem.* **2012**, *22*, 13268.

(5) Bai, X.; Ji, H. M.; Gao, P.; Zhang, Y.; Sun, X. H. Morphology, Phase Structure and Acetone Sensitive Properties of Copper-Doped Tungsten Oxide Sensors. *Sens. Actuators, B* **2014**, *193*, 100−106.

(6) Wang, Z. Y.; Sun, P.; Yang, T. L.; Gao, Y.; Li, X. W.; Lu, G. Y.; Du, Y. Flower-Like WO_3 Architectures Synthesized Via a Microwave-Assisted Method and Their Gas Sensing Properties. *Sens. Actuators, B* **2013**, *186*, 734−740.

(7) Vuong, N. M.; Jung, H.; Kim, D.; Kim, H.; Hong, S. K. Realization of an Open Space Ensemble for Nanowires: A Strategy for the Maximum Response in Resistive Sensors. *J. Mater. Chem.* **2012**, *22*, 6716−6725.

(8) Bai, S. L.; Zhang, K. W.; Luo, R. X.; Li, D. Q.; Chen, A. F.; Liu, C. C. Low-Temperature Hydrothermal Synthesis of WO_3 Nanorods and Their Sensing Properties for NO_2. *J. Mater. Chem.* **2012**, *22*, 12643−12650.

(9) Ponzoni, A.; Russo, V.; Bailini, A.; Casari, C. S.; Ferroni, M.; Bassi, A. L.; Migliori, A.; Morandi, V.; Ortolani, L.; Sberveglieri, G.; Bottani, C. E. Structural and Gas-Sensing Characterization of Tungsten Oxide Nanorods and Nanoparticles. *Sens. Actuators, B* **2011**, *153*, 340−346.

(10) Chen, D. L.; Hou, X. X.; Li, T.; Yin, L.; Fan, B. B.; Wang, H. L.; Li, X. J.; Xu, H. L.; Lu, H. X.; Zhang, R.; Sun, J. Effects of Morphologies on Acetone-Sensing Properties of Tungsten Trioxide Nanocrystals. *Sens. Actuators, B* **2011**, *153*, 373−381.

(11) Zhang, J.; Liu, X. H.; Xu, M. J.; Guo, X. Z.; Wu, S. H.; Zhang, S. M.; Wang, S. R. Pt Clusters Supported on WO_3 for Ethanol Detection. *Sens. Actuators, B* **2010**, *147*, 185−190.

(12) Szilagyi, I. M.; Saukko, S.; Mizsei, J.; Toth, A. L.; Madarasz, J.; Pokol, G. Gas Sensing Selectivity of Hexagonal and Monoclinic WO_3 to H_2S. *Solid State Sci.* **2010**, *12*, 1857−1860.

(13) Senguttuvan, T. D.; Srivastava, V.; Tawal, J. S.; Mishra, M.; Srivastava, S.; Jain, K. Gas Sensing Properties of Nanocrystalline Tungsten Oxide Synthesized by Acid Precipitation Method. *Sens. Actuators, B* **2010**, *150*, 384−388.

(14) Jimenez, I.; Centeno, M. A.; Scotti, R.; Morazzoni, F.; Arbiol, J.; Cornet, A.; Morante, J. R. NH_3 Interaction with Chromium-Doped WO_3 Nanocrystalline Powders for Gas Sensing Applications. *J. Mater. Chem.* **2004**, *14*, 2412−2420.

(15) Qamar, M.; Gondal, M. A.; Yamani, Z. H. Synthesis of Highly Active Nanocrystalline WO_3 and Its Application in Laser-Induced Photocatalytic Removal of a Dye from Water. *Catal. Commun.* **2009**, *10*, 1980−1984.

(16) Martinez-de la Cruz, A.; Martinez, D. S.; Cuellar, E. L. Synthesis and Characterization of WO_3 Nanoparticles Prepared by the Precipitation Method: Evaluation of Photocatalytic Activity under Vis-Irradiation. *Solid State Sci.* **2010**, *12*, 88−94.

(17) Martinez, D. S.; Martinez-de la Cruz, A.; Cuellar, E. L. Photocatalytic Properties of WO_3 Nanoparticles Obtained by Precipitation in Presence of Urea as Complexing Agent. *Appl. Catal., A* **2011**, *398*, 179−186.

(18) Zhang, X. H.; Lu, X. H.; Shen, Y. Q.; Han, J. B.; Yuan, L. Y.; Gong, L.; Xu, Z.; Bai, X. D.; Wei, M.; Tong, Y. X.; Gao, Y. H.; Chen, J.; Zhou, J.; Wang, Z. L. Three-Dimensional WO_3 Nanostructures on Carbon Paper: Photoelectrochemical Property and Visible Light Driven Photocatalysis. *Chem. Commun.* **2011**, *47*, 5804−5806.

(19) Szilagyi, I. M.; Forizs, B.; Rosseler, O.; Szegedi, A.; Nemeth, P.; Kiraly, P.; Tarkanyi, G.; Vajna, B.; Varga-Josepovits, K.; Laszlo, K.; Toth, A. L.; Baranyai, P.; Leskela, M. WO_3 Photocatalysts: Influence of Structure and Composition. *J. Catal.* **2012**, *294*, 119−127.

(20) Cong, S.; Tian, Y.; Li, Q.; Zhao, Z.; Geng, F. Single-Crystalline Tungsten Oxide Quantum Dots for Fast Pseudocapacitor and Electrochromic Applications. *Adv. Mater. (Weinheim, Ger.)* **2014**, *26*, 4260−7.

(21) Yoon, S.; Kang, E.; Kim, J. K.; Lee, C. W.; Lee, J. Development of High-Performance Supercapacitor Electrodes Using Novel Ordered Mesoporous Tungsten Oxide Materials with High Electrical Conductivity. *Chem. Commun.* **2011**, *47*, 1021−1023.

(22) Wang, Y. H.; Wang, C. C.; Cheng, W. Y.; Lu, S. Y. Dispersing WO_3 in Carbon Aerogel Makes an Outstanding Supercapacitor Electrode Material. *Carbon* **2014**, *69*, 287−293.
(23) Figueroa, R.; Cruz, T. G. S.; Gorenstein, A. WO_3 Pillar-Type and Helical-Type Thin Film Structures to Be Used in Microbatteries. *J. Power Sources* **2007**, *172*, 422−427.
(24) Galiote, N. A.; Parreira, R. L. T.; Rosolen, J. M.; Huguenin, F. Self-Assembled Films from WO_3: Electrochromism and Lithium Ion Diffusion. *Electrochem. Commun.* **2010**, *12*, 733−736.
(25) Li, W. J.; Fu, Z. W. Nanostructured WO_3 Thin Film as a New Anode Material for Lithium-Ion Batteries. *Appl. Surf. Sci.* **2010**, *256*, 2447−2452.
(26) Santos, L.; Neto, J. P.; Crespo, A.; Nunes, D.; Costa, N.; Fonseca, I. M.; Barquinha, P.; Pereira, L.; Silva, J.; Martins, R.; Fortunato, E. WO_3 Nanoparticle-based Conformable pH Sensor. *ACS Appl. Mater. Interfaces* **2014**, *6*, 12226−34.
(27) Zheng, H. D.; Ou, J. Z.; Strano, M. S.; Kaner, R. B.; Mitchell, A.; Kalantar-Zadeh, K. Nanostructured Tungsten Oxide - Properties, Synthesis, and Applications. *Adv. Funct. Mater.* **2011**, *21*, 2175−2196.
(28) Santato, C.; Odziemkowski, M.; Ulmann, M.; Augustynski, J. Crystallographically Oriented Mesoporous WO_3 Films: Synthesis, Characterization, and Applications. *J. Am. Chem. Soc.* **2001**, *123*, 10639−10649.
(29) Iwu, K. O.; Galeckas, A.; Rauwel, P.; Kuznetsov, A. Y.; Norby, T. One-Dimensional WO_3 and Its Hydrate: One-Step Synthesis, Structural and Spectroscopic Characterization. *J. Solid State Chem.* **2012**, *185*, 245−252.
(30) Yu, J. G.; Yu, H. G.; Guo, H. T.; Li, M.; Mann, S. Spontaneous Formation of a Tungsten Trioxide Sphere-in-Shell Superstructure by Chemically Induced Self-Transformation. *Small* **2008**, *4*, 87−91.
(31) Wang, L. S.; Pfeifer, J.; Balazsi, C.; Gouma, P. I. Synthesis and Sensing Properties to NH_3 of Hexagonal WO_3 Metastable Nanopowders. *Mater. Manuf. Processes* **2007**, *22*, 773−776.
(32) Qin, Y. X.; Bao, Z. Y.; Hu, M.; Zhang, J. Synthesis and NO_2-Sensing Properties of One-Dimensional Tungsten Oxide Nanowire Bundles. *J. Nanosci. Nanotechnol.* **2011**, *11*, 11142−11146.
(33) Polleux, J.; Pinna, N.; Antonietti, M.; Niederberger, M. Growth and Assembly of Crystalline Tungsten Oxide Nanostructures Assisted by Bioligation. *J. Am. Chem. Soc.* **2005**, *127*, 15595−15601.
(34) Polleux, J.; Gurlo, A.; Barsan, N.; Weimar, U.; Antonietti, M.; Niederberger, M. Template-Free Synthesis and Assembly of Single-Crystalline Tungsten Oxide Nanowires and Their Gas-Sensing Properties. *Angew. Chem., Int. Ed.* **2006**, *45*, 261−265.
(35) Pokhrel, S.; Simion, C. E.; Teodorescu, V. S.; Barsan, N.; Weimar, U. Synthesis, Mechanism, and Gas-Sensing Application of Surfactant Tailored Tungsten Oxide Nanostructures. *Adv. Funct. Mater.* **2009**, *19*, 1767−1774.
(36) Xi, G. C.; Ouyang, S. X.; Li, P.; Ye, J. H.; Ma, Q.; Su, N.; Bai, H.; Wang, C. Ultrathin $W_{18}O_{49}$ Nanowires with Diameters Below 1 nm: Synthesis, near-Infrared Absorption, Photoluminescence, and Photochemical Reduction of Carbon Dioxide. *Angew. Chem., Int. Ed.* **2012**, *51*, 2395−2399.
(37) Choi, H. G.; Jung, Y. H.; Kim, D. K. Solvothermal Synthesis of Tungsten Oxide Nanorod/Nanowire/Nanosheet. *J. Am. Ceram. Soc.* **2005**, *88*, 1684−1686.
(38) Lou, X. W.; Zeng, H. C. An Inorganic Route for Controlled Synthesis of $W_{18}O_{49}$ Nanorods and Nanofibers in Solution. *Inorg. Chem.* **2003**, *42*, 6169−6171.
(39) Yang, T. S.; Zhang, Y.; Li, C. Chemical and Structural Analysis of Solvothermal Synthesized Tungsten Oxide Nanotube without Template and Its Hydrogen Sensitive Property. *J. Alloys Compd.* **2014**, *584*, 546−552.
(40) Zhang, H. Y.; Huang, C. L.; Tao, R. T.; Zhao, Y. F.; Chen, S.; Sun, Z. Y.; Liu, Z. M. One-Pot Solvothermal Method to Synthesize Platinum/$W_{18}O_{49}$ Ultrafine Nanowires and Their Catalytic Performance. *J. Mater. Chem.* **2012**, *22*, 3354−3359.
(41) Qin, Y. X.; Li, X.; Wang, F.; Hu, M. Solvothermally Synthesized Tungsten Oxide Nanowires/Nanorods for NO_2 Gas Sensor Applications. *J. Alloys Compd.* **2011**, *509*, 8401−8406.
(42) Zhao, Z.-G.; Miyauchi, M. Nanoporous-Walled Tungsten Oxide Nanotubes as Highly Active Visible-Light-Driven Photocatalysts. *Angew. Chem., Int. Ed.* **2008**, *47*, 7051−7055.
(43) Li, X. L.; Lou, T. J.; Sun, X. M.; Li, Y. D. Highly Sensitive WO_3 Hollow-Sphere Gas Sensors. *Inorg. Chem.* **2004**, *43*, 5442−5449.
(44) Epifani, M.; Andreu, T.; Arbiol, J.; Diaz, R.; Siciliano, P.; Morante, J. R. Chloro-Alkoxide Route to Transition Metal Oxides. Synthesis of WO_3 Thin Films and Powders from a Tungsten Chloro-Methoxide. *Chem. Mater.* **2009**, *21*, 5215−5221.
(45) Daniel, M. F.; Desbat, B.; Lassegues, J. C.; Gerand, B.; Figlarz, M. Infrared and Raman-Study of WO_3 Tungsten Trioxides and WO_3, xH_2O Tungsten Trioxide Hydrates. *J. Solid State Chem.* **1987**, *67*, 235−247.
(46) Salje, E. Lattice Dynamics of WO_3. *Acta Crystallogr., Sect. A: Cryst. Phys., Diffr., Theor. Gen. Crystallogr.* **1975**, *31*, 360−363.
(47) Lee, D. H.; Condrate, R. A. FTIR Spectral Characterization of Thin Film Coatings of Oleic Acid on Glasses: I. Coatings on Glasses from Ethyl Alcohol. *J. Mater. Sci.* **1999**, *34*, 139−146.
(48) Young, A. G.; Al-Salim, N.; Green, D. P.; McQuillan, A. J. Attenuated Total Reflection Infrared Studies of Oleate and Trioctylphosphine Oxide Ligand Adsorption and Exchange Reactions on CdS Quantum Dot Films. *Langmuir* **2008**, *24*, 3841−3849.
(49) Yu, W. W.; Wang, Y. A.; Peng, X. G. Formation and Stability of Size-, Shape-, and Structure-Controlled CdTe Nanocrystals: Ligand Effects on Monomers and Nanocrystals. *Chem. Mater.* **2003**, *15*, 4300−4308.
(50) Seo, J. W.; Jun, Y. W.; Ko, S. J.; Cheon, J. In Situ One-Pot Synthesis of 1-Dimensional Transition Metal Oxide Nanocrystals. *J. Phys. Chem. B* **2005**, *109*, 5389−5391.
(51) Lee, K.; Seo, W. S.; Park, J. T. Synthesis and Optical Properties of Colloidal Tungsten Oxide Nanorods. *J. Am. Chem. Soc.* **2003**, *125*, 3408−3409.
(52) Johansson, M. B.; Baldissera, G.; Valyukh, I.; Persson, C.; Arwin, H.; Niklasson, G. A.; Osterlund, L. Electronic and Optical Properties of Nanocrystalline WO_3 Thin Films Studied by Optical Spectroscopy and Density Functional Calculations. *J. Phys.: Condens. Matter* **2013**, *25*, 205502.
(53) Chang, G.; Xu, M. Research Progress and Potential Application of WO_3 Electrochromic Films. *Mater. Eng. Technol.* **2014**, *849*, 373−379.
(54) Allen, E. A.; Brisdon, B. J.; Edwards, D. A.; Fowles, G. W. A.; Williams, R. G. 890. Halide and Oxyhalide Complexes of Molybdenum and Tungsten. *J. Chem. Soc.* **1963**, 4649−4657.
(55) Kon, H.; Sharpless, N. E. Electron Spin Resonance Study of Some Halomolybdenyl, -Tungstenyl, and -Vanadyl Complexes in Solution. *J. Phys. Chem.* **1966**, *70*, 105−111.
(56) Nagiev, V. M. Factors Influencing the Concentration of V (IV) Complexes and the Parameters of the Spin Hamiltonian in Phosphate-Vanadate Semiconducting Glasses. *J. Struct. Chem.* **1976**, *17*, 859−865.
(57) Judeinstein, P.; Livage, J. Sol-Gel Synthesis of WO_3 Thin-Films. *J. Mater. Chem.* **1991**, *1*, 621−627.
(58) Klejnot, O. J. Chloride Alkoxides of Pentavalent Tungsten. *Inorg. Chem.* **1965**, *4*, 1668−1670.
(59) Ho, S. F.; Contarini, S.; Rabalais, J. W. Ion-Beam-Induced Chemical-Changes in the Oxyanions (MO_y^{n-}) and Oxides (MO_x) Where M = Cr, Mo, W, V, Nb, and Ta. *J. Phys. Chem.* **1987**, *91*, 4779−4788.
(60) Shpak, A. P.; Korduban, A. M.; Medvedskij, M. M.; Kandyba, V. O. XPS Studies of Active Elements Surface of Gas Sensors Based on WO_{3-X} Nanoparticles. *J. Electron Spectrosc. Relat. Phenom.* **2007**, *156*, 172−175.
(61) Xie, F. Y.; Gong, L.; Liu, X.; Tao, Y. T.; Zhang, W. H.; Chen, S. H.; Meng, H.; Chen, J. XPS Studies on Surface Reduction of Tungsten Oxide Nanowire Film by Ar^+ Bombardment. *J. Electron Spectrosc. Relat. Phenom.* **2012**, *185*, 112−118.
(62) Yamazoe, N.; Shimanoe, K. Theory of Power Laws for Semiconductor Gas Sensors. *Sens. Actuators, B* **2008**, *128*, 566−573.
(63) You, L.; He, X.; Wang, D.; Sun, P.; Sun, Y. F.; Liang, X. S.; Du, Y.; Lu, G. Y. Ultrasensitive and Low Operating Temperature NO_2 Gas

Sensor Using Nanosheets Assembled Hierarchical WO_3 Hollow Microspheres. *Sens. Actuators, B* **2012**, *173*, 426−432.
(64) You, L.; Sun, Y. F.; Ma, J.; Guan, Y.; Sun, J. M.; Du, Y.; Lu, G. Y. Highly Sensitive NO_2 Sensor Based on Square-Like Tungsten Oxide Prepared with Hydrothermal Treatment. *Sens. Actuators, B* **2011**, *157*, 401−407.
(65) Qin, Y. X.; Shen, W. J.; Li, X.; Hu, M. Effect of Annealing on Microstructure and NO_2-Sensing Properties of Tungsten Oxide Nanowires Synthesized by Solvothermal Method. *Sens. Actuators, B* **2011**, *155*, 646−652.
(66) Meng, D.; Yamazaki, T.; Shen, Y. B.; Liu, Z. F.; Kikuta, T. Preparation of WO_3 Nanoparticles and Application to NO_2 Sensor. *Appl. Surf. Sci.* **2009**, *256*, 1050−1053.
(67) Liu, Z. F.; Miyauchi, M.; Yamazaki, T.; Shen, Y. B. Facile Synthesis and NO_2 Gas Sensing of Tungsten Oxide Nanorods Assembled Microspheres. *Sens. Actuators, B* **2009**, *140*, 514−519.
(68) Barsan, N.; Weimar, U. Conduction Model of Metal Oxide Gas Sensors. *J. Electroceram.* **2001**, *7*, 143−167.
(69) Oison, V.; Saadi, L.; Lambert-Mauriat, C.; Hayn, R. Mechanism of CO and O_3 Sensing on WO_3 Surfaces: First Principle Study. *Sens. Actuators, B* **2011**, *160*, 505−510.
(70) Saadi, L.; Lambert-Mauriat, C.; Oison, V.; Ouali, H.; Hayn, R. Mechanism of NO_x Sensing on WO_3 Surface: First Principle Calculations. *Appl. Surf. Sci.* **2014**, *293*, 76−79.
(71) Kohl, D. Surface Processes in the Detection of Reducing Gases with SnO_2-Based Devices. *Sens. Actuators, B* **1989**, *18*, 71−113.
(72) Zeng, W.; Li, Y. Q.; Miao, B.; Pan, K. G. Hydrothermal Synthesis and Gas Sensing Properties of $WO_3{\cdot}H_2O$ with Different Morphologies. *Phys. E (Amsterdam, Neth.)* **2014**, *56*, 183−188.
(73) Upadhyay, S. B.; Mishra, R. K.; Sahay, P. P. Structural and Alcohol Response Characteristics of Sn-Doped WO_3 Nanosheets. *Sens. Actuators, B* **2014**, *193*, 19−27.
(74) Li, J.; Zhu, J. W.; Liu, X. H. Synthesis, Characterization and Enhanced Gas Sensing Performance of WO_3 Nanotube Bundles. *New J. Chem.* **2013**, *37*, 4241−4249.
(75) Ahmad, M. Z.; Sadek, A.; Ou, J. Z.; Yaacob, M. H.; Latham, K.; Wlodarski, W. Facile Synthesis of Nanostructured WO_3 Thin Films and Their Characterization for Ethanol Sensing. *Mater. Chem. Phys.* **2013**, *141*, 912−919.
(76) Zhang, H. J.; Liu, T. M.; Huang, L.; Guo, W. W.; Liu, D. J.; Zeng, W. Hydrothermal Synthesis of Assembled Sphere-like WO_3 Architectures and Their Gas-Sensing Properties. *Phys. E (Amsterdam, Neth.)* **2012**, *44*, 1467−1472.
(77) Vallejos, S.; Stoycheva, T.; Umek, P.; Navio, C.; Snyders, R.; Bittencourt, C.; Llobet, E.; Blackman, C.; Moniz, S.; Correig, X. Au Nanoparticle-Functionalised WO_3 Nanoneedles and Their Application in High Sensitivity Gas Sensor Devices. *Chem. Commun.* **2011**, *47*, 565−567.
(78) Ma, J. M.; Zhang, J.; Wang, S. R.; Wang, T. H.; Lian, J. B.; Duan, X. C.; Zheng, W. J. Topochemical Preparation of WO_3 Nanoplates through Precursor H_2WO_4 and Their Gas-Sensing Performances. *J. Phys. Chem. C* **2011**, *115*, 18157−18163.
(79) Huang, J. R.; Xu, X. J.; Gu, C. P.; Yang, M.; Yang, M.; Liu, J. H. Large-Scale Synthesis of Hydrated Tungsten Oxide 3D Architectures by a Simple Chemical Solution Route and Their Gas-Sensing Properties. *J. Mater. Chem.* **2011**, *21*, 13283−13289.
(80) Hoa, N. D.; El-Safty, S. A. Gas Nanosensor Design Packages Based on Tungsten Oxide: Mesocages, Hollow Spheres, and Nanowires. *Nanotechnology* **2011**, *22*, 485503.
(81) Su, X. T.; Li, Y. I.; Jian, J. K.; Wang, J. D. In Situ Etching WO_3 Nanoplates: Hydrothermal Synthesis, Photoluminescence and Gas Sensor Properties. *Mater. Res. Bull.* **2010**, *45*, 1960−1963.
(82) Chen, D. L.; Hou, X. X.; Wen, H. J.; Wang, Y.; Wang, H. L.; Li, X. J.; Zhang, R.; Lu, H. X.; Xu, H. L.; Guan, S. K.; Sun, J.; Gao, L. The Enhanced Alcohol-Sensing Response of Ultrathin WO_3 Nanoplates. *Nanotechnology* **2010**, *21*, 035501.